A Highly Sensitive Single Crystal Perovskite–Graphene Hybrid Vertical Photodetector

Yuting Zou, Tingting Zou, Chen Zhao, Bin Wang, Jun Xing, Zhi Yu, Jinluo Cheng, Wei Xin, Jianjun Yang, Weili Yu,* Huanli Dong, and Chunlei Guo*

Organolead trihalide perovskites have attracted significant attention for optoelectronic applications due to their excellent physical properties in the past decade. Generally, both grain boundaries in perovskite films and the device structure play key roles in determining the device performance, especially for horizontal-structured device. Here, the first optimized vertical-structured photodetector with the perovskite single crystal MAPbBr$_3$ as the light absorber and graphene as the transport layer is shown. The hybrid device combines strong photoabsorption characteristics of perovskite and high carrier mobility of flexible graphene, exhibits excellent photoresponse performance with high photoresponsivity ($\approx$1017.1 A W^{-1}) and high photodetectivity ($\approx$2.02 $\times$ 10^{13} Jones) in a low light intensity (0.66 mW cm^{-2}) under the actuations of 3 V bias and laser irradiation at 532 nm. In particular, an ultrahigh photoconductive gain of $\approx$2.37 $\times$ 10^3 is attained because of fast charge transfer in the graphene and large recombination lifetime in the perovskite single crystal. The vertical architecture combining perovskite crystal with highly conductive graphene offers opportunities to fulfill the synergistic effect of perovskite and 2D materials, is thus promising for developing high-performance electronic and optoelectronic devices.

1. Introduction

Photodetectors have attracted extensive attention in the field of academic and industrial in recent decades owing to their

wide application in optical communication, environmental monitoring, biological detection, image sensing, space exploration and other fields.[1–5] Recently, methylammonium lead halide (CH$_3$NH$_3$PbX$_3$, X = halogen) perovskites have become promising candidate materials as building blocks for light harvesting in photodetectors due to their excellent photoelectric properties, including direct bandgap, wide spectral response (UV-NIR), large absorption coefficient ($\approx$10^5 cm^{-1}), high power conversion (22.7%), high carrier mobility ($\approx$100 cm^2 V^{-1} s^{-1}), long carrier diffusion length ($\approx$0.1–10 μm) and small exciton-binding energy ($\approx$20 meV).[6–12] As a result, this class of material has been widely applied in photoelectric devices such as solar cells,[13–15] light-emitting diodes (LED),[16–18] lasers,[19–21] and field-effect transistor.[22–24]

To date, some groups have reported the excellent performance of perovskite photodetectors with high gains, ultra-sensitivity, ultra-fast response speed or wavelength selection.[25–28] Although solution-processed perovskite thin film photodetectors have made great achievements in recent years, their performance is adversely affected by mass defects in the surface and grain boundaries of the polycrystalline film.[29,30] The grain boundaries of polycrystalline film will hinder the charge transport in the horizontal direction and weaken the charge coupling, thus lead to poor charge transport properties and low charge carrier mobility. Due to the adverse effects of defects in perovskite polycrystalline films, it is necessary to passivation the defects or traps to obtain devices with better performance. So many studies have combined perovskite with high mobility 2D materials to increase responsivity, with the perovskite as the photosensitive layer and the 2D materials as the transport layer. In 2015, Cho and co-workers[31] and others prepared a new type of hybrid photodetector consisting of graphene and solution-based MAPbI$_3$ perovskite, which showed a wide spectral response from 400 to 800 nm; and in the same year, Bao and co-workers[32] reported a wide-spectrum heterojunction photodetector with monolayer graphene covered with a thin layer of dispersive organolead halide perovskite (CH$_3$NH$_3$PbBr$_2$I) islands. Thereafter, Lee and co-workers[33] demonstrated a highly sensitive hybrid photodetector based on graphene-CsPbBr$_{3-x}$I$_x$ perovskite nanocrystals. Zeng's group fabricated a broad absorption spectrum photodetectors with 2D MoS$_2$ layer and all-inorganic CsPbBr$_3$ perovskite
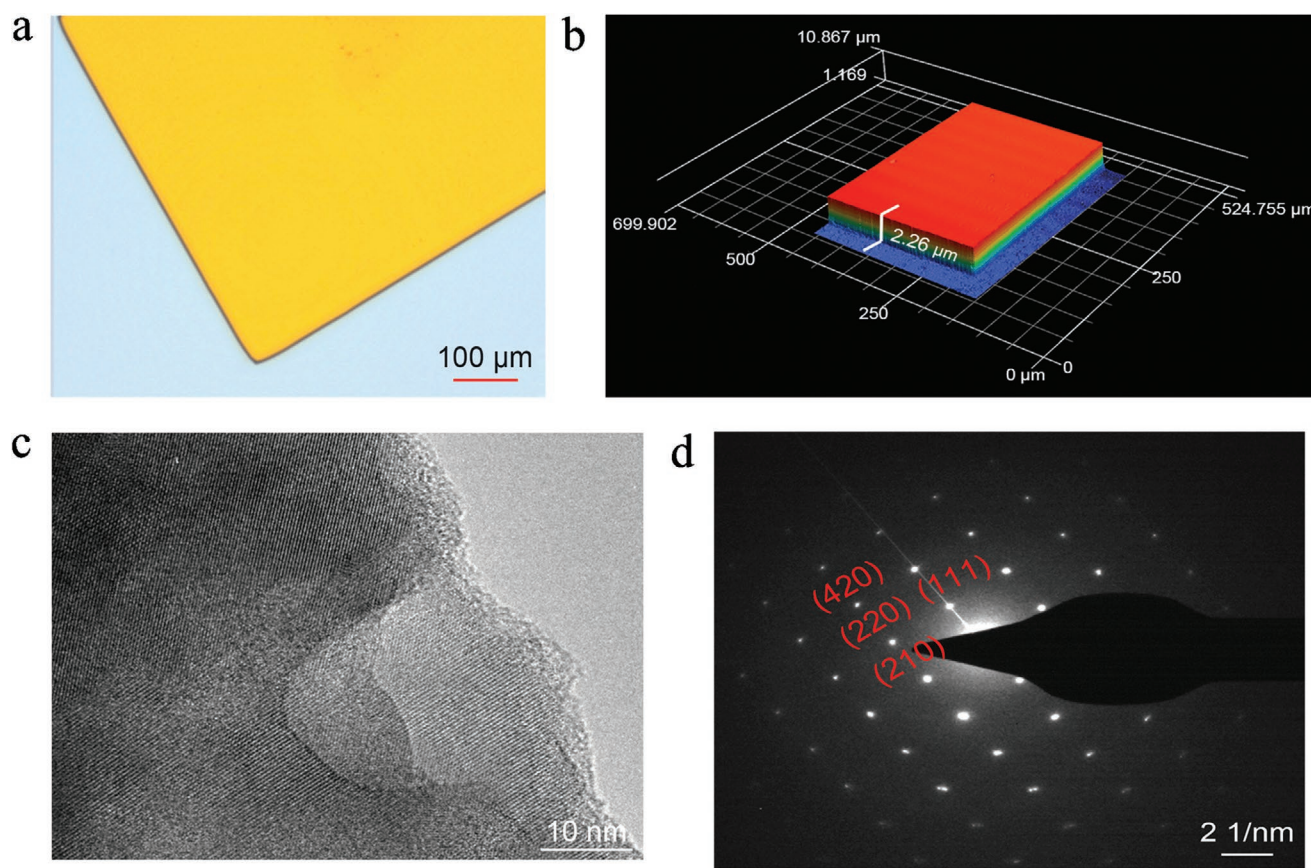
Y. Zou, T. Zou, C. Zhao, B. Wang, J. Xing, Dr. Z. Yu, Prof. J. Cheng, Dr. W. Xin, Prof. J. Yang, Prof. W. Yu, Prof. C. Guo
The Guo Photonics Laboratory, State Key Laboratory of Applied Optics
Changchun Institute of Optics, Fine Mechanics and Physics (CIOMP)
Chinese Academy of Sciences (CAS)
Changchun 130033, P. R. China
E-mail: weili.yu@ciomp.ac.cn
Y. Zou, T. Zou, C. Zhao, B. Wang, J. Xing
University of Chinese Academy of Sciences
Beijing 100049, P. R. China
Prof. H. Dong
Beijing National Laboratory for Molecular Science
Key Laboratory of Organic Solids
Beijing 100190, P. R. China
Prof. C. Guo
The Institute of Optics
University of Rochester
Rochester, NY 14627, USA
E-mail: chunlei.guo@rochester.edu

The ORCID identification number(s) for the author(s) of this article can be found under https://doi.org/10.1002/smll.202000733.

**ADVANCED
SCIENCE NEWS**

www.advancedsciencenews.com

NANO · MICRO

small

www.small-journal.com

Figure 1. a) Optical image of MAPbBr$_3$ single crystal grown by ITC method (scale bar: 100 µm). b) 3D pseudo color plot of MAPbBr$_3$ single crystal thickness, the thickness is 2.25 microns. c) TEM photograph and d) SAED pattern of MAPbBr$_3$ single crystal.

nanosheets.[34] In 2019, Wei Lin Leong attained an ultrahigh photoconductive gain CsPbBr$_x$I$_{3-x}$ nanocrystal-graphene hybrid photodetector.[35] Although the performance of perovskite-2D materials hybrid photodetector has been greatly improved, the negative effects of grain boundary have not been resolved.

Herein, we report the first vertical-structured photodetector, which combines monolayer graphene with a perovskite single crystal MAPbBr$_3$ as light collection material together. Taking the advantages of graphene's ultrahigh carrier mobility and single crystal perovskite with low defects and high absorption coefficient, the graphene–perovskite hybrid vertical photodetector exhibits excellent photoresponse, i.e., an approximately order of magnitude enhancement of photoresponsivity ($\approx$1017.1 A W^{-1}), photodetectivity ($\approx$2.02 × 10^{13} Jones) and photoconductive gain ($\approx$2.37 × 10^3) at 532 nm. The enhanced performance of vertical photodetector can be attributed to the effective extraction of free charges by graphene and the high carrier mobility of graphene with high flexibility.[31,32] Our work shows that the hybrid graphene–perovskite vertical photodetector has broad application prospects in high-performance optoelectronic devices.

2. Discussion

We synthesized the high-quality MAPbBr$_3$ single crystal by the inverse temperature crystallization (ITC) method.[36] **Figure 1a** shows the optical image of the MAPbBr$_3$ single crystal, from which we can see that the surface of this single crystal is smooth and the edge is regular. In Figure S1a (Supporting Information), a scanning electron microscope (SEM) image of MAPbBr$_3$ single crystal shows the surface is flat and smooth without grain boundary. The Energy dispersive X-ray spectrometry (EDS) of the selected area was measured (Figure S1b, Supporting Information) and the four elements including carbon (C), nitrogen (N), lead (Pb), and bromine (Br) are evenly distributed, which demonstrated its high crystalline quality. This high crystallinity facilitates the efficient transport of carriers, resulting in excellent device performance. By controlling the concentration of the precursor solution and crystallization speed, a centimeter-size single crystal with the thickness of several micrometers can be obtained on the silicon substrate. As shown in Figure 1b, the thickness of the single crystal is about 2.3 µm measured by laser confocal microscope. Figure 1c,d display the transmission electron microscope (TEM) image and selected area electron diffraction (SAED) pattern of the perovskite single crystal, from which the MAPbBr$_3$ single crystal shows regular crystal structure and evenly distributed reflection matrix, implying the high quality of MAPbBr$_3$ single crystal synthesized. The high quality single crystal with smooth surface ensures that MAPbBr$_3$ single crystal can minimize the contact resistance with Au electrodes and the charge can be effectively transported in the channel.
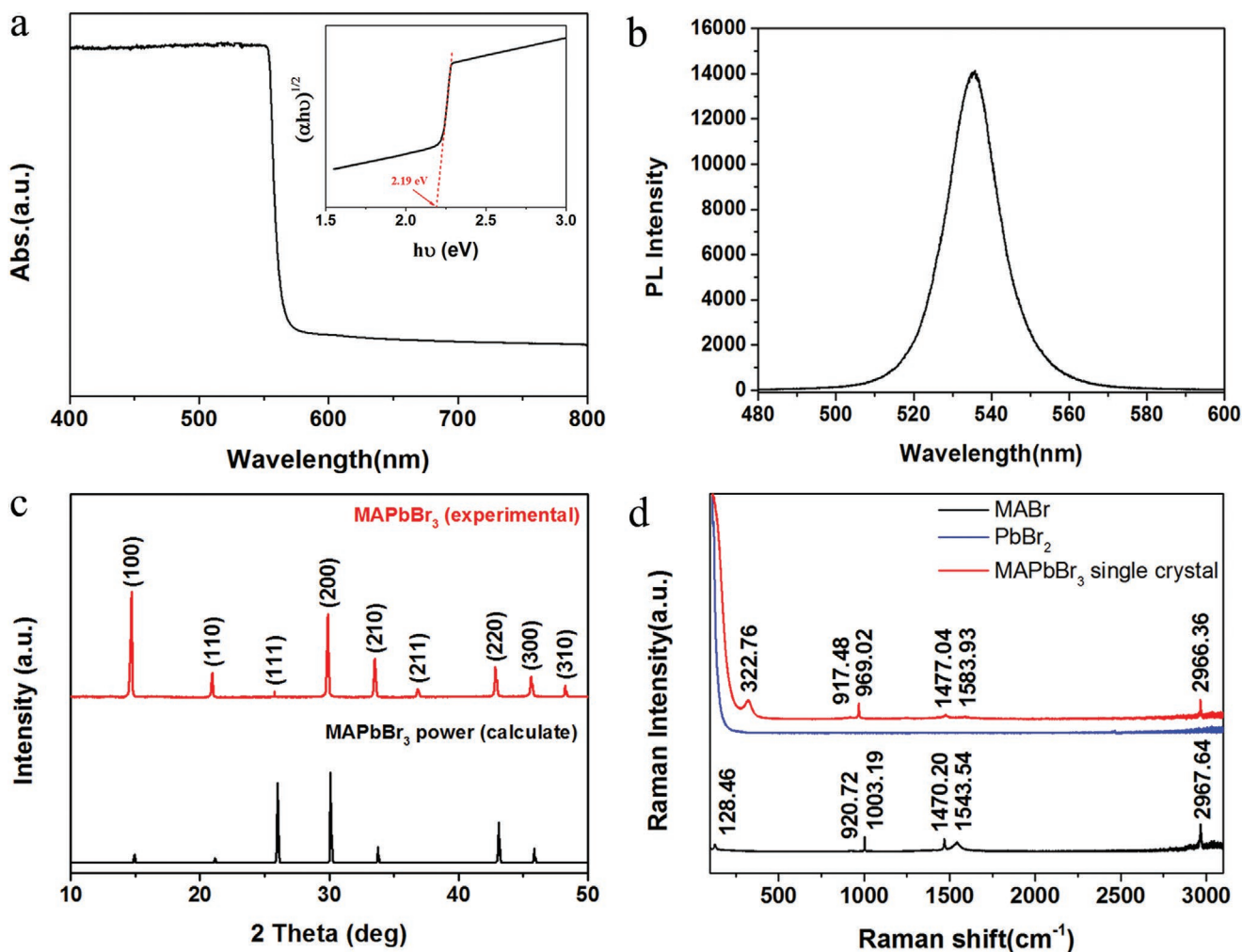
Figure 2. a) The UV–vis pattern of MAPbBr$_3$ single crystal; Inset: Tauc plot from UV–vis analysis of MAPbBr$_3$ single crystal to calculate bandgap energy. b) Photoluminescence spectra of MAPbBr$_3$ single crystal with the excitation of 473 nm laser. c) The experimental and calculated powder X-ray diffraction (XRD) patterns of MAPbBr$_3$ single crystal. d) Raman spectra of MABr, PbBr$_2$ and MAPbBr$_3$ single crystal with the excitation of 785 nm laser.

In order to further characterize the crystallinity of the MAPbBr$_3$ single crystal, we measured the electrical properties of the perovskite single crystal by absorption, steady-state fluorescence, X-ray diffraction and Raman spectrum, respectively. **Figure 2**a shows the UV–vis spectrum of MAPbBr$_3$ single crystal. According to the absorption spectra, the bandgap energy (E_g) is calculated to be 2.19 eV by the Tauc Plots method.[37] Figure 2b presents the PL spectrum which was excited by 473 nm laser and displays a narrow peak at 535 nm. The power X-ray diffraction (XRD) spectrum of MAPbBr$_3$ single crystal is shown in Figure 2c, it indicates that MAPbBr$_3$ single crystal is cubic structure which is in well agreement with the theoretical calculation.[38] Figure 2d displays the Raman spectra of MABr, PbBr$_2$, and MAPbBr$_3$ single crystal, from the spectra we can conclude that the MABr and PbBr$_2$ reacted completely and pure MAPbBr$_3$ single crystal formed.

Based on the silicon substrate covered by a monolayer graphene with high carrier mobility, hybrid graphene–perovskite single crystal vertical photodetector is prepared, as shown in **Figure 3**a. In this hybrid vertical photodetector, the monolayer graphene is used as the charge transport layer and perovskite single crystal as the photoabsorption layer. The typical metal-semiconductor-mental (MSM) model, being the so-called photoconductor type, was fabricated, which also helps to analyze the process of photoresponse. The detailed process of device preparation can be found in Section S3 in the Supporting Information. Monolayer graphene synthesized on the surface of copper foil by chemical vapor deposition (CVD) method[39] was transferred to a pretreated Si/SiO$_2$ (250 nm) substrate with the aid of polymethyl methacrylate (PMMA) polymer (Figure S2a, Supporting Information).[40] We characterized the Raman spectra of the monolayer graphene transferred onto a Si/SiO$_2$ substrate. As shown in Figure S2b (Supporting Information), the Raman spectrum has two distinct peaks, which are located at 1585.3 cm^{-1} for G peak and 2701.06 cm^{-1} for 2D peak, respectively. And the ratio of 2D peak and G peak is 2.438,[41] which proved that the transferred graphene has good quality and smooth surface. So it can be well contacted with MAPbBr$_3$ single crystal. Then the gold electrodes were evaporated on the prepared graphene. Subsequently, the MAPbBr$_3$ single crystal
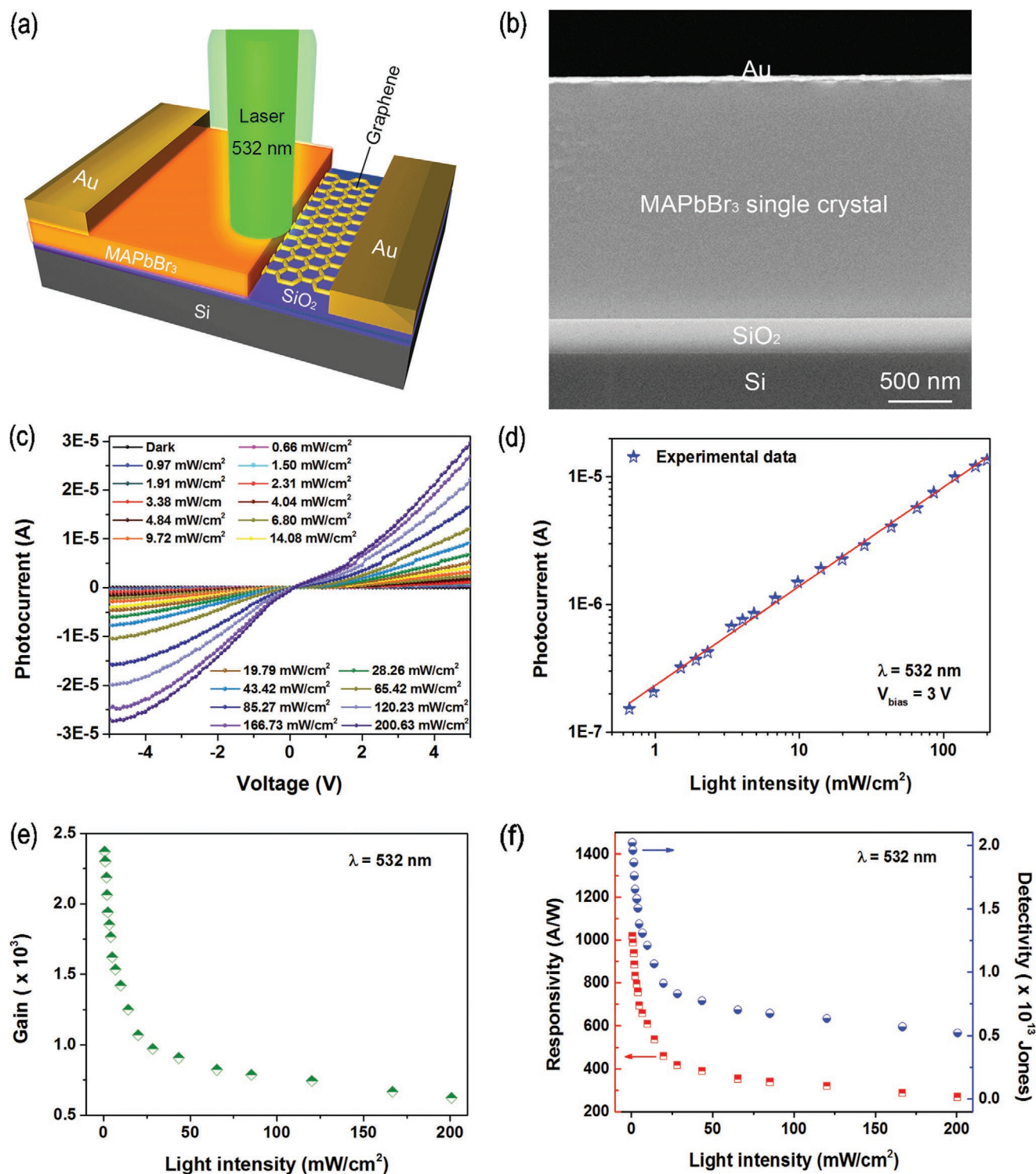
Figure 3. a) Schematic of the graphene–perovskite vertical photodetector. b) Cross-sectional SEM diagram of the device. c) *I–V* characteristics of the device under 532 nm light illumination with various light intensities. d) Photocurrent as a function of the incident light intensity at 3 V. e) Gain, and f) responsivity and detectivity as a function of incident light intensity.

were grown on the monolayer graphene by ITC. Finally, the soft contact gold electrode was transferred on the top of the perovskite single crystal by the probe method[42] to complete the fabrication of the entire device. The mechanical-transfer-gold-electrode technology provides an efficient method for fabricating vertical electronic and optoelectronic devices, solving the difficulty of preparing top-contact metal electrodes and preventing Au electrodes from penetrating into the active layer.[43]
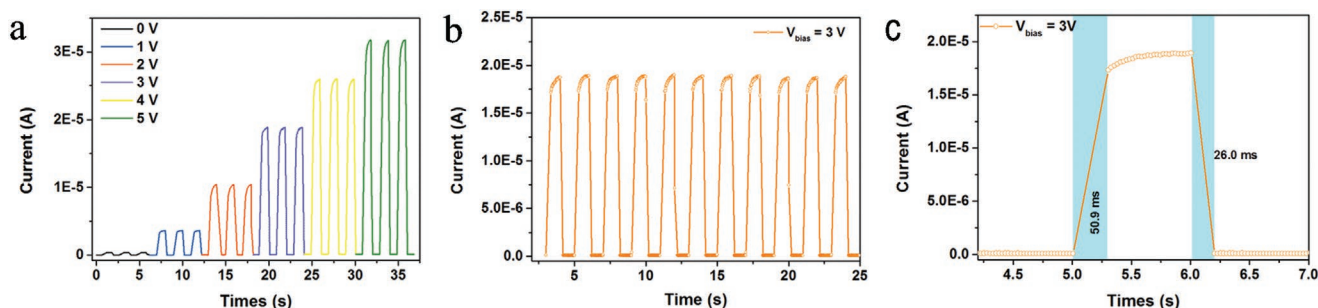
ADVANCED
SCIENCE NEWS
www.advancedsciencenews.com

NANO · MICRO
small
www.small-journal.com

Figure 4. a) Time–dependent photoresponse under 532 nm light illumination with reverse bias voltages (200.63 mW cm^{-2}). b,c) The photoswitch of the graphene – perovskite vertical photodetector.

Figure 3b shows the cross-sectional SEM image of the structure of the device, i.e., graphene–perovskite single crystal-metal vertical heterostructure. The interface between each layer is distinct and has no penetration, especially the interface between gold electrode and MAPbBr$_3$ single crystal, which indicates the high interface quality of this device. The electrical properties of the hybrid graphene–perovskite vertical photodetector were measured at room temperature under atmospheric conditions. We characterized the photoresponse of the hybrid vertical photodetector. As plotted in Figure 3c, the nearly linear current-voltage performance indicates that there is a good ohmic contact between gold electrode and the graphene–perovskite. By carefully studying the I–V characteristics of the device with different light intensities at 532 nm (Figure 3c), one can observe a phenomenon that the photocurrent increases gradually with increasing light intensity. This phenomenon can be attributed to the increase in the number of photogenerated carriers as the light intensity increasing. The dependence of photocurrent on light intensity can be understood by a power law, $I_{ph} \propto P^{\theta}$, where I_{ph} is the photocurrent, P is the light intensity and θ is the index, which determines the recombination of the photocarriers. As shown in Figure 3d, the fitting curve in a wide light intensity range shows that $\theta = 0.76$, indicating that the composite loss is relatively low in this range.[44]

Next, we calculated three important parameters of a photodetector, which are photoresponsivity (R), photodetectivity (D*), and photoconductive gain (G). The parameter R refers to the photocurrent generated by the unit power of the incident light on the effective area and is expressed by the following equation[45]

$$R = \frac{I_{light} - I_{dark}}{P \cdot A} \qquad (1)$$

where I_{light}, I_{dark}, P, and A are the photocurrent, dark current, incident light power, and effective illumination area of the device, respectively. The parameter G represents the number of charge carrier detected relative to the number of photogenerated electron–hole pairs, which is usually given by[45]

$$G = R \frac{hc}{e\lambda} \qquad (2)$$

where R is photoresponsivity, h is Planck's constant, c is the light velocity, e is the elementary charge, and λ is wavelength of incident light.

And to characterize the sensitivity of the device, when the dark current is dominated by the shot noise,[46] determine the detectivity (D*) value was determined using the equation below

$$D^* = \frac{R}{\sqrt{2q \, J_{dark}}} \qquad (3)$$

where R is the photoresponsivity and J_{dark} is the dark current density of the photodetector. According to the above formula, when the bias was given as 3 V, R, D* and G were estimated to be as high as ≈1017.1 A W^{-1}, ≈2.02 × 10^{13} Jones, and ≈2.37 × 10^3 electrons per photon at light intensity of ≈0.66 mW cm^{-2}. The R, D* and G value is higher than that of photodetector based on pure perovskite, which the details are shown in Figure S4 (Supporting Information). And the relationship between photoresponsivity and light intensity can be fitted with a power function, as shown in Figure 3f. This relationship can be analyzed using a model of carrier recombination in photovoltaic devices. As the carrier density increases, the probability of carrier recombination increases, which is one of the reasons for the decrease in the response rate of light intensity.

In addition, photoresponse is another crucial performance parameter of a photodetector. As shown in **Figure 4**a, the time-dependent photoresponse demonstrates that the sensitivity to the incident light is highly repeatable and stable. In addition, as the bias voltage increasing, the photocurrent monotonically increases, which is understandable because a large electric field can promote the effective transport of photocarriers and reduce their composite activity. And Figure 4b presents the rising and falling edges are very steep, indicating a fast response. The rise time and decay time are 50.9 and 26 ms, respectively, which are comparable to previous reports,[32,47] as shown in Figure 4c.

For comparison, the photodetectors based on pure MAPbBr$_3$ single crystal were studied (the detailed information can be found in Section S4 in the Supporting Information). **Figure 5**a compares the I–V characteristics of pure perovskite and graphene–perovskite heterostructures under illumination with the laser irradiation (532 nm, 200.63 mW cm^{-2}), respectively. In order to further assess the performance of the hybrid graphene–perovskite device, we compared the photoresponsivity, detectivity and photoconductive gain, being three critical parameters at 532 nm laser irradiation. Figure 5b–d respectively show the photoresponsivity (R), detectivity (D*) and photoconductive gain (G) comparison of the as-fabricated vertical photodetector at 532 nm laser with the bias of 3 V. It can be seen
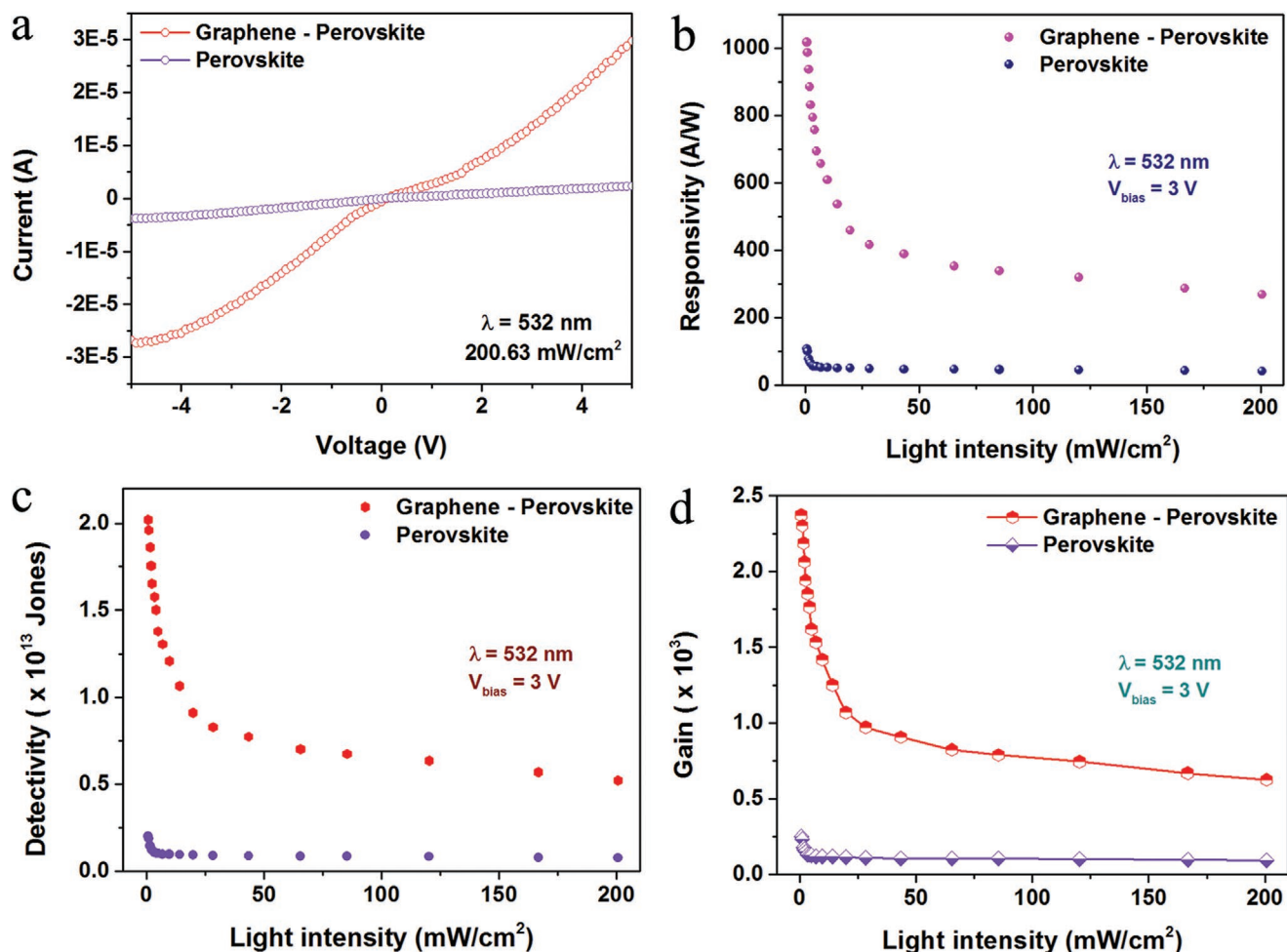
ADVANCED
SCIENCE NEWS
www.advancedsciencenews.com

NANO · MICRO
small
www.small-journal.com

Figure 5. a) *I–V* characteristics of the perovskite and graphene–perovskite vertical photodetectors under 532 nm illumination. b–d) The responsivity, detectivity, and gain of the perovskite and graphene – perovskite vertical photodetectors under 532 nm illumination at 3 V bias.

that the above parameters are increased by an order for hybrid graphene–perovskite photodetector. The device performance is greatly enhanced due to the effective charge transfer from the graphene to perovskite. When graphene and perovskite are in contact, their Fermi energy levels are not consistent. In order to make the Fermi energy levels of the system consistent and reach the thermal equilibrium state, the holes in graphene will diffuse into the perovskite energy levels, leaving electrons in the

graphene and causing electron doping.[32,35] Due to the charge transfer, the built–in electric field is formed, which makes the perovskite band bend upward and provides the driving force for the separation and transfer of photogenerated electron–hole pairs.[32,48,49,50] As shown in **Figure 6**a, under light illumination, perovskite absorbs light and excites electron–hole pairs. Due to the mismatch of work functions of graphene and perovskite, electron–hole pairs were separated by the internal electric field.
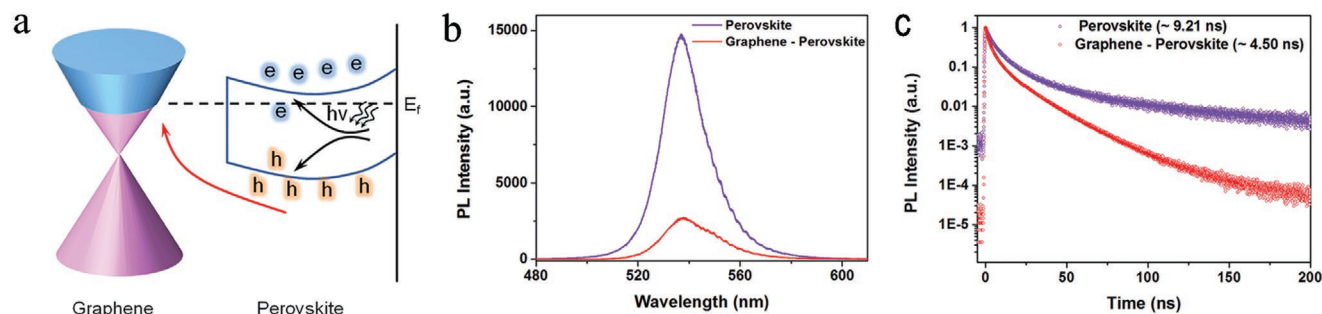

Figure 6. a) Energy band diagram of graphene–perovskite vertical device under illumination. b) PL spectra of MAPbBr$_3$ single crystal and MAPbBr$_3$ single crystal on graphene. c) PL lifetime of MAPbBr$_3$ single crystal and MAPbBr$_3$ single crystal on graphene.

Table 1. Performance comparison of perovskite-based photodetectors.

Material structure	Light wavelength (nm)/power	R [mA W^{-1}]	D^* [Jones]	Gain	Ref.
MAPbI$_3$/Graphene (G)	520/1×10^{-3} mW	1.8×10^5	10^9	–	[31]
MAPbI$_3$ island/G/Au NPs	532/1.4×10^{-2} mW cm^{-2}	2.1×10^6	–	–	[54]
MAPbI$_3$ nanowire/graphene	633/3.3 pW	2841	2.6×10^9	–	[55]
MAPbI$_3$/rGO	520/3.2 mW cm^{-2}	73.9	–	–	[56]
CsPbBr$_x$I$_{3-x}$ nanocrystal/Graphene	525/80 μW cm^{-2}	1.13×10^7	1.17×10^{11}	9.32×10^{10}	[35]
MAPbBr$_2$I/Graphene	405/921.5 nW	6.0×10^8	–	$\approx 10^9$	[32]
MAPbI$_3$ microwires/Graphene	520/13.5 mW cm^{-2}	2.2	1.78×10^5	–	[57]
FA$_{0.85}$Cs$_{0.15}$PbI$_3$/Graphene	650/25.1 mW cm^{-2}	4.8×10^3	4.2×10^{12}	–	[58]
2D perovskite/MoS$_2$	532/1.6 mW cm^{-2}	$\approx 10^7$	4.0×10^{10}	–	[59]
FA$_{0.85}$Cs$_{0.15}$PbI$_3$/DNTT	450/46 nW cm^{-2}	7.78×10^5	1.04×10^{13}	2.1×10^3	[60]
MAPbBr$_3$ single crystal/Graphene	532/0.66 mW cm^{-2}	1.07×10^6	2.02×10^{13}	2.37×10^3	Our work

And the holes are transferred to graphene because of the interfacial electric field, while the electrons are bound to perovskite and act as an additional light tunable gate. The electric field generated by these electrons causes holes in the graphene to be induced, lowering the Fermi energy level of graphene and further increasing the photocurrent.[12,51] And Figure 6b showed the steady-state PL spectra of the perovskite and hybrid graphene–perovskite samples, which were prepared on Si substrates with 250 nm SiO$_2$.

Under the same experimental conditions, PL peaks of perovskite and hybrid graphene perovskite appeared at around 535 nm. However, the PL quantum yield of hybrid graphene–perovskite is much lower than that of the original perovskite single crystal. The dramatic PL quenching is caused by the effective charge carrier transfer caused by π–π interaction between the perovskite and the sp^2 hybridized graphene layer.[31] Generally, in the absence of graphene, photoinduced electron–hole pairs in perovskite tend to recombine within the lifetime; however, electrons in the graphene layer were transferred to the proximal perovskite layer to fill the vacancy in the perovskite valence band due to photon absorption. Therefore, the recombination of the photoexcited electron–hole pairs in the perovskite was limited, and therefore, the photoexcited electrons in the perovskite remained in the conduction band without decaying. The process of trapping photoexcited electrons is the main mechanism of the observation of a dramatic quenching of the PL intensity in the hybrid graphene–perovskite system.[52] It is worth mentioning that in this unique device geometry, the recombination of photoexcited electrons and holes was greatly suppressed, because electrons can be effectively extracted from the perovskite layer, which increases the photocurrent. A time-resolved photoluminescence (TRPL) dynamics were also performed to obtain a quantitative analysis of charge injection and separation (see Figure 6c). When excited at 532 nm, the hybrid graphene–perovskite shows much shorter lifetime, with an average lifetime of 4.50 ns, as compared to that of the original perovskite (9.21 ns). The result demonstrates a substantial charge extraction and transfer from MAPbBr$_3$ single crystal to graphene and therefore facilitating an efficient photoresponse.

There are several strategies to improve the performance of perovskite optoelectronic devices. The commonly used ones include interface modification, multicomponent doping and crystal morphology transformation. A detailed comparison of these methods is summarized in **Table 1**. By comparison, we believe that the method presented here is competitive in enhancing the performance of perovskite vertical photodetectors. In addition, owing to the relatively mature graphene transfer technology and single crystal growth technology, our method is compatible with other optimization methods, and has unique advantages in the actual industrial integration.

3. Conclusion

In conclusion, we demonstrated a novel hybrid vertical photodetector consisting of monolayer graphene and MAPbBr$_3$ single crystal. Comparing to photodetector based on pure perovskite single crystal, the hybrid vertical photodetector showed an order of magnitude enhancement in the photoresponsivity ($\approx$1017.1 A W^{-1}), photodetectivity ($\approx$2.02 $\times$ 10^{13} Jones), photoconductive gain ($\approx$2.37 $\times$ 10^3) at 3 V bias under 200 mW cm^{-2} laser actuation (532 nm). The enhanced performance can be attributed to the effective charge transfer from the graphene to perovskite and heterojunction formed between graphene and perovskite. Graphene photodetectors based on organic-inorganic hybrid lead halide can be further developed by introducing alternative organic bonds or halide groups to meet the requirements of some specific applications.[53] The hybrid photodetectors described herein are expected to facilitate the development of imaging sensors for low light photography, UV detectors with high response, and smart skin sensors that combine with other functions.

4. Experimental Section

Chemicals: Methylamine solution (40% aqueous solution, Aladdin), lead bromide (PbBr$_2$) (99%, Aladdin), *N*,*N*-dimethylformamide (DMF) (99.5%,Aladdin), hydrobromic acid (HBr) (40% aqueous solution), ethanol absolute, and diethyl ether were all purchased from Sinopharm Chemical Reagent Co., Ltd. without further purification.

**ADVANCED
SCIENCE NEWS**

www.advancedsciencenews.com

**NANO · MICRO
small**

www.small-journal.com

Synthesis Methylammonium Bromide (MABr): The MABr was synthesized by the reaction of HBr with methylamine solution, and then recrystallized from absolute ethanol and diethyl ether. First, CH_3NH_3 (61 mL) was poured into a round bottom flask and hydrobromic acid (56 mL) in a constant pressure funnel was slowly dropped into CH_3NH_3. After all the hydrobromic acid was added, the mixed solution was placed in an ice water bath for 2 h. Then the mixture was poured into a rotary flask for rotary evaporation at 60 °C, when the clear liquid became white power, it was washed with absolute ethanol for three times. Finally the MABr was placed in a vacuum drying box and dried at 60 °C for 24 h.

Synthesis MAPbBr$_3$ Single Crystal: The substrate (Si/SiO$_2$) and the covering glass were washed successively with deionized water, ethanol, acetone, and isopropanol. After being dried in a drying box at 100 °C, the substrate and the covering glass were placed in UV–O$_3$ for hydrophilic treatment. The covered glass was immersed in a mixed solution of hexane and OTS (600:1) to obtain a hydrophobic surface, and then the glass was rinsed with acetone for 30 s and then dried with nitrogen. A small amount (5 µL) of MAPbBr$_3$ precursor solution was dropped onto the silicon substrate and then covered it with covering glass. Then the sandwich structure sheet was put on a hotplate, which slowly heated from 40 to 100 °C.

Characterization: The UV–vis absorption spectra of MAPbBr$_3$ single crystal was measured with a Cary 5000 spectrophotometer from Agilent Company. Raman spectra of MABr, PbBr$_2$ and MAPbBr$_3$ single crystal were measured by using a HORIBA Scientific Raman spectrometer with a 785 nm laser. PL spectra were measured by a HORIBA Scientific Raman spectrometer with 2.55 mW cm^{-2} laser intensity at 473 nm in air at room temperature. Optical image of the perovskite single crystal was performed on a Nikon SMZ25 stereomicroscope. The thickness of the single crystal was performed on a Keyence laser confocal microscope (VK-X1000). The SEM image of cross-sectional was obtained from a Hitachi S-4800. The crystal structure was characterized by X-ray diffraction with Bruker D8 Focus.

Hybrid Vertical Photodetector Fabrication and Characterization: To fabricate hybrid vertical photodetector, monolayer graphene synthesized on the surface of copper foil by chemical vapor deposition (CVD) was efficiently transferred to a heavily doped, n-type Si/SiO$_2$ (250 nm) substrate with the polymethyl methacrylate (PMMA) polymer. Then 80 nm gold source electrode was evaporated on the single-layer graphene and perovskite MAPbBr$_3$ single crystal were grown on the monolayer graphene by ITC method. Finally, the soft contact gold electrode was transferred onto the top of the perovskite single crystal.

All the I–V curves were measured at room temperature in the ambient atmosphere with a Keithley 4200A Semiconductor Parametric Analyzer (Tektronix) and a C-100 probe station from TPSi – Company. All the photoresponse characteristics of the devices were measured by a 532 nm laser with tunable light intensity from 0.6 to 200 mW cm^{-2}. The exposure time of the sample was precisely controlled by an optical shutter (VS25S2TO, UNIBLITZ) with a diameter of 2.5 mm.

Supporting Information

Supporting Information is available from the Wiley Online Library or from the author.

Acknowledgements

Conflict of Interest

The authors declare no conflict of interest.

[1] G. Konstantatos, E. H. Sargent, *Nat. Nanotechnol.* **2010**, *5*, 885.
[2] F. H. Koppens, T. Mueller, P. Avouris, A. C. Ferrari, M. S. Vitiello, M. Polini, *Nat. Nanotechnol.* **2014**, *9*, 780.
[3] R. D. Jansen-van Vuuren, A. Armin, A. K. Pandey, P. L. Burn, P. Meredith, *Adv. Mater.* **2016**, *28*, 4766.
[4] A. Armin, R. D. Jansen-van Vuuren, N. Kopidakis, P. L. Burn, P. Meredith, *Nat. Commun.* **2015**, *6*, 6343.
[5] L. Zhou, R. Wang, C. Yao, X. Li, C. Wang, X. Zhang, C. Xu, A. Zeng, D. Zhao, F. Zhang, *Nat. Commun.* **2015**, *6*, 6938.
[6] G. C. Xing, N. Mathews, S. Y. Sun, S. S. Lim, Y. M. Lam, M. Gratzel, S. Mhaisalkar, T. C. Sum, *Science* **2013**, *342*, 344.
[7] S. D. Stranks, G. E. Eperon, G. Grancini, C. Menelaou, M. J. P. Alcocer, T. Leijtens, L. M. Herz, A. Petrozza, H. J. Snaith, *Science* **2013**, *342*, 341.
[8] C. Wehrenfennig, G. E. Eperon, M. B. Johnston, H. J. Snaith, L. M. Herz, *Adv. Mater.* **2014**, *26*, 1584.
[9] S. D. Stranks, H. J. Snaith, *Nat. Nanotechnol.* **2015**, *10*, 391.
[10] O. Malinkiewicz, A. Yella, Y. H. Lee, G. M. Espallargas, M. Graetzel, M. K. Nazeeruddin, H. J. Bolink, *Nat. Photonics* **2014**, *8*, 128.
[11] H. Wang, D. H. Kim, *Chem. Soc. Rev.* **2017**, *46*, 5204.
[12] X. Hu, X. Zhang, L. Liang, J. Bao, S. Li, W. Yang, Y. Xie, *Adv. Funct. Mater.* **2014**, *24*, 7373.
[13] W. Yu, F. Li, H. Wang, E. Alarousu, Y. Chen, B. Lin, L. Wang, M. N. Hedhili, Y. Li, K. Wu, X. Wang, O. F. Mohammed, T. Wu, *Nanoscale* **2016**, *8*, 6173.
[14] H. H. Fang, F. Wang, S. Adjokatse, N. Zhao, J. Even, M. Antonietta Loi, *Light: Sci. Appl.* **2016**, *5*, 16056.
[15] D. W. deQuilettes, S. M. Vorpahl, S. D. Stranks, H. Nagaoka, G. E. Eperon, M. E. Ziffer, H. J. Snaith, D. S. Ginger, *Science* **2015**, *348*, 683.
[16] N. Wang, L. Cheng, R. Ge, S. Zhang, Y. Miao, W. Zou, C. Yi, Y. Sun, Y. Cao, R. Yang, Y. Wei, Q. Guo, Y. Ke, M. Yu, Y. Jin, Y. Liu, Q. Ding, D. Di, L. Yang, G. Xing, H. Tian, C. Jin, F. Gao, R. H. Friend, J. Wang, W. Huang, *Nat. Photonics* **2016**, *10*, 699.
[17] A. B. Wong, M. Lai, S. W. Eaton, Y. Yu, E. Lin, L. Dou, A. Fu, P. Yang, *Nano Lett.* **2015**, *15*, 5519.
[18] Z. K. Tan, R. S. Moghaddam, M. L. Lai, P. Docampo, R. Higler, F. Deschler, M. Price, A. Sadhanala, L. M. Pazos, D. Credgington, F. Hanusch, T. Bein, H. J. Snaith, R. H. Friend, *Nat. Nanotechnol.* **2014**, *9*, 687.
[19] T. Kondo, T. Azuma, T. Yuasa, R. Ito, *Solid State Commun.* **1998**, *105*, 253.
[20] B. R. Sutherland, S. Hoogland, M. M. Adachi, C. T. O. Wong, E. H. Sargent, *ACS Nano* **2014**, *8*, 10947.
[21] A. Fu, P. Yang, *Nat. Mater.* **2015**, *14*, 557.
[22] Y. Zou, F. Li, C. Zhao, J. Xing, Z. Yu, W. Yu, C. Guo, *Adv. Opt. Mater.* **2019**, *7*, 1900676.
[23] W. Yu, F. Li, L. Yu, M. R. Niazi, Y. Zou, D. Corzo, A. Basu, C. Ma, S. Dey, M. L. Tietze, U. Buttner, X. Wang, Z. Wang, M. N. Hedhili, C. Guo, T. Wu, A. Amassian, *Nat. Commun.* **2018**, *9*, 5354.
[24] F. Li, C. Ma, H. Wang, W. Hu, W. Yu, A. D. Sheikh, T. Wu, *Nat. Commun.* **2015**, *6*, 8238.
[25] L. Dou, Y. M. Yang, J. You, Z. Hong, W. H. Chang, G. Li, Y. Yang, *Nat. Commun.* **2014**, *5*, 5404.
[26] R. Dong, Y. Fang, J. Chae, J. Dai, Z. Xiao, Q. Dong, Y. Yuan, A. Centrone, X. C. Zeng, J. Huang, *Adv. Mater.* **2015**, *27*, 1912.

[27] L. Shen, Y. Fang, D. Wang, Y. Bai, Y. Deng, M. Wang, Y. Lu, J. Huang, *Adv. Mater.* **2016**, *28*, 10794.

[28] M. I. Saidaminov, M. A. Haque, M. Savoie, A. L. Abdelhady, N. Cho, I. Dursun, U. Buttner, E. Alarousu, T. Wu, O. M. Bakr, *Adv. Mater.* **2016**, *28*, 8144.

[29] T. S. Sherkar, C. Momblona, L. Gil-Escrig, J. Avila, M. Sessolo, H. J. Bolink, L. J. A. Koster, *ACS Energy Lett.* **2017**, *2*, 1214.

[30] J.-W. Lee, S.-H. Bae, N. De Marco, Y.-T. Hsieh, Z. Dai, Y. Yang, *Mater. Today Energy* **2018**, *7*, 149.

[31] Y. Lee, J. Kwon, E. Hwang, C. H. Ra, W. J. Yoo, J. H. Ahn, J. H. Park, J. H. Cho, *Adv. Mater.* **2015**, *27*, 41.

[32] Y. Wang, Y. Zhang, Y. Lu, W. Xu, H. Mu, C. Chen, H. Qiao, J. Song, S. Li, B. Sun, Y.-B. Cheng, Q. Bao, *Adv. Opt. Mater.* **2015**, *3*, 1389.

[33] D.-H. Kwak, D.-H. Lim, H.-S. Ra, P. Ramasamy, J.-S. Lee, *RSC Adv.* **2016**, *6*, 65252.

[34] X. F. Song, X. H. Liu, D. J. Yu, C. X. Huo, J. P. Ji, X. M. Li, S. L. Zhang, Y. S. Zou, G. Y. Zhu, Y. J. Wang, M. Z. Wu, A. Xie, H. B. Zeng, *ACS Appl. Mater. Interfaces* **2018**, *10*, 2801.

[35] A. Surendran, X. Yu, R. Begum, Y. Tao, Q. J. Wang, W. L. Leong, *ACS Appl. Mater. Interfaces* **2019**, *11*, 27064.

[36] M. I. Saidaminov, A. L. Abdelhady, B. Murali, E. Alarousu, V. M. Burlakov, W. Peng, I. Dursun, L. Wang, Y. He, G. Maculan, A. Goriely, T. Wu, O. F. Mohammed, O. M. Bakr, *Nat. Commun.* **2015**, *6*, 7586.

[37] J. B. Coulter, D. P. Birnie, *Phys. Status Solidi B* **2018**, *255*, 1700393.

[38] Y. Liu, Y. Zhang, Z. Yang, J. Feng, Z. Xu, Q. Li, M. Hu, H. Ye, X. Zhang, M. Liu, K. Zhao, S. Liu, *Mater. Today* **2019**, *22*, 67.

[39] X. S. Li, W. W. Cai, J. H. An, S. Kim, J. Nah, D. X. Yang, R. Piner, A. Velamakanni, I. Jung, E. Tutuc, S. K. Banerjee, L. Colombo, R. S. Ruoff, *Science* **2009**, *324*, 1312.

[40] A. Reina, X. T. Jia, J. Ho, D. Nezich, H. Son, V. Bulovic, M. Dresselhaus, J. Kong, *Nano Lett.* **2009**, *9*, 30.

[41] L. Jiang, T. Niu, X. Lu, H. Dong, W. Chen, Y. Liu, W. Hu, D. Zhu, *J. Am. Chem. Soc.* **2013**, *135*, 9050.

[42] Q. Tang, L. Jiang, Y. Tong, H. Li, Y. Liu, Z. Wang, W. Hu, Y. Liu, D. Zhu, *Adv. Mater.* **2008**, *20*, 2947.

[43] H. Haick, D. Cahen, *Acc. Chem. Res.* **2008**, *41*, 359.

[44] Z. X. Zhang, L. H. Zeng, X. W. Tong, Y. Gao, C. Xie, Y. H. Tsang, L. B. Luo, Y. C. Wu, *J. Phys. Chem. Lett.* **2018**, *9*, 1185.

[45] C. Xie, C. Mak, X. Tao, F. Yan, *Adv. Funct. Mater.* **2017**, *27*, 1603886.

[46] Z. Yang, Y. Deng, X. Zhang, S. Wang, H. Chen, S. Yang, J. Khurgin, N. X. Fang, X. Zhang, R. Ma, *Adv. Mater.* **2018**, *30*, 1704333.

[47] Y. Yu, Y. Zhang, Z. Zhang, H. Zhang, X. Song, M. Cao, Y. Che, H. Dai, J. Yang, J. Wang, H. Zhang, J. Yao, *J. Phys. Chem. Lett.* **2017**, *8*, 445.

[48] J. N. Yun, H. D. Fan, Y. N. Zhang, R. J. Huang, Y. B. Ren, M. Z. Guo, H. An, P. Kang, H. Guo, *ACS Appl. Mater. Interfaces* **2020**, *12*, 3086.

[49] K. P. Bera, G. Haider, Y. T. Huang, P. K. Roy, C. R. P. Inbaraj, Y. M. Liao, H. Lin, C. H. Lu, C. Shen, W. Y. Shih, W. H. Shih, Y. F. Chen, *ACS Nano* **2019**, *13*, 12540.

[50] A. Surendran, X. C. Yu, R. Begum, Y. Tao, Q. J. Wang, *ACS Appl. Mater. Interfaces* **2019**, *11*, 27064.

[51] Y. Q. Huang, R. J. Zhu, N. Kang, J. Du, H. Q. Xu, *Appl. Phys. Lett.* **2013**, *103*, 143119.

[52] J. T. Wang, J. M. Ball, E. M. Barea, A. Abate, J. A. Alexander-Webber, J. Huang, M. Saliba, I. Mora-Sero, J. Bisquert, H. J. Snaith, R. J. Nicholas, *Nano Lett.* **2014**, *14*, 724.

[53] N.-G. Park, *J. Phys. Chem. Lett.* **2013**, *4*, 2423.

[54] Z. Sun, L. Aigouy, Z. Chen, *Nanoscale* **2016**, *8*, 7377.

[55] M. Spina, M. Lehmann, B. Nafradi, L. Bernard, E. Bonvin, R. Gaal, A. Magrez, L. Forro, E. Horvath, *Small* **2015**, *11*, 4824.

[56] M. He, Y. Chen, H. Liu, J. Wang, X. Fang, Z. Liang, *Chem. Commun.* **2015**, *51*, 9659.

[57] J. Ding, H. J. Fang, Z. P. Lian, Q. R. Lv, J. L. Sun, Q. F. Yan, *Nanoscale* **2018**, *10*, 10538.

[58] C. Y. Wu, Z. Wang, L. Liang, T. Gui, W. Zhong, R. C. Du, C. Xie, L. Wang, L. B. Luo, *Small* **2019**, *15*, 1900730.

[59] Q. Fu, X. Wang, F. Liu, Y. Dong, Z. Liu, S. Zheng, A. Chaturvedi, J. Zhou, P. Hu, Z. Zhu, F. Bo, Y. Long, Z. Liu, *Small* **2019**, *15*, 1902890.

[60] L. B. Luo, G. A. Wu, Y. Gao, L. Liang, C. Xie, Z. X. Zhang, X. W. Tong, T. Wang, F. X. Liang, *Adv. Opt. Mater.* **2019**, *7*, 1900272.